

# Symmetry breaking, snap-through, and pull-in instabilities under dynamic loading of microelectromechanical shallow arches

**K Das and R C Batra**

Department of Engineering Science and Mechanics, M/C 0219  
Virginia Polytechnic Institute and State University  
Blacksburg, VA 24061, USA

E-mails: [kdas@vt.edu](mailto:kdas@vt.edu), [rbatra@vt.edu](mailto:rbatra@vt.edu)

**Abstract.** Arch-shaped microelectromechanical systems (MEMS) have been used as mechanical memories, micro-relays, micro-valves, optical switches, and digital micro-mirrors. A bi-stable structure, such as an arch, is characterized by a multivalued load deflection curve. Here we study the symmetry breaking, the snap-through instability, and the pull-in instability of a bi-stable arch shaped MEMS under static and dynamic electric loads. Unlike a mechanical load, the electric load is a nonlinear function of the *a priori* unknown deformed shape of the arch. The nonlinear partial differential equation governing transient deformations of the arch is solved numerically using the Galerkin method and a time integration scheme that adaptively adjusts the time step to compute the solution within the prescribed tolerance. For the static problem, the displacement control and the pseudo-arc length continuation methods are used to obtain the bifurcation curve of arch's displacement versus a load parameter. The displacement control method fails to compute arch's asymmetric deformations that are found by the pseudo-arc-length continuation method. For the dynamic problem, two distinct mechanisms of the snap-through instability are found. It is shown that critical loads and geometric parameters for instabilities of an arch under an electric load with and without the consideration of mechanical inertia effects are quite different. A phase diagram between a critical load parameter and the arch height is constructed to delineate different regions of instabilities. We compare results from the present model with those from a continuum mechanics based approach, and with results of other models and experiments available in the literature.

## **Key words**

Symmetry breaking, pull-in parameters, snap-through instability, bi-stability, pseudo-arc-length continuation

## **1. Introduction**

An electrically actuated microelectromechanical system (MEMS) consists of a deformable electrode made of a conductive material suspended above a rigid conductive

electrode with a dielectric medium, generally air, between them (figure 1). An electric potential difference applied between the two electrodes induces the Coulomb pressure on the electrodes, which deflects the deformable electrode towards the rigid one. The elastic restoring force induced in the deformed electrode restricts its motion. Electric charges redistribute on the deformable electrode's surface as the gap between it and the rigid electrode decreases, which in turn increases the Coulomb pressure and deflects the deformable electrode more until the Coulomb pressure balances the elastic restoring force. MEMS of dimensions in the range of a few to a hundred micrometers are used as radio frequency (RF) switches, varactors and inductors [37], accelerometers [38], pressure sensors, controllers for micro-mirrors [42], micro-pumps [4], and bio-MEMS [2].

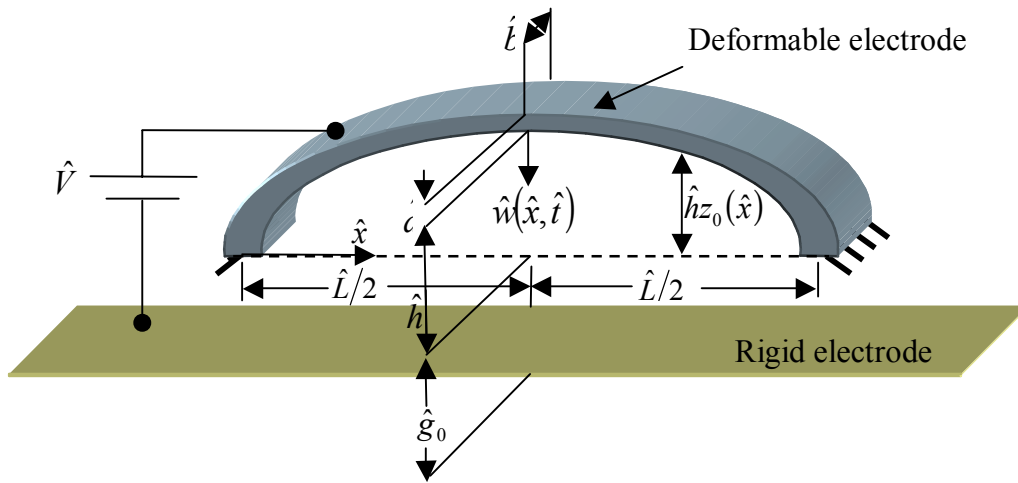


Figure 1. Schematic sketch of the problem studied.

### 1.1 The pull-in Instability in MEMS

For electrically actuated MEMS, the applied electric potential has an upper limit, beyond which the elastic restoring force does not balance the corresponding Coulomb force resulting in collapse of the deformable electrode on the rigid one. This phenomenon, called the pull-in instability, was observed experimentally by Taylor [41] and Nathanson et al. [28]. The corresponding values of the potential difference and the peak deflection of

the deformable electrode are called the pull-in voltage and the pull-in deflection, respectively. Collectively, they are known as the pull-in parameters.

Accurate estimates of pull-in parameters are crucial for designing electrically actuated MEMS. In switching applications [30], the pull-in instability is necessary for the switch to operate. However, for micro-mirrors [20] and micro-resonators [26] the pull-in instability restricts the range of operational displacement of the device.

### *1.2 The snap-through instability in an arch shaped MEMS*

In an arch shaped deformable electrode such as that shown in figure 1, in addition to the pull-in instability, the snap-through instability can occur under the Coulomb pressure. Depending upon the initial elevation  $\hat{h}$ , either snap-through or pull-in instability or both instabilities occur. Advantages of the snap-through instability have been exploited in actuators [43, 44, 39, 31], microvalves [17], and transducers [25]. The snap-through instability of an arch shaped MEMS under slowly applied electric loads has been observed experimentally and studied with reduced order models in [46, 23, 24, 21]. Various conditions such as arch rise  $\hat{h}$  (see figure 1), arch thickness  $\hat{d}$ , type of loads (step or ramp), and gap  $\hat{g}_0$  between the electrodes determine whether the snap-through will occur. Pippard [34] and Patricio et al. [32] have presented a phase diagram between the arch length and the initial arch angle at the clamped end, showing conditions for which the snap-through can occur due to a quasistatic deflection-independent point load. Krylov et al. [21] have presented a phase diagram between  $\hat{h}$  and  $\hat{d}$  depicting conditions for which the snap-through can occur in static deflections of a bell shaped MEMS. Depending on the arch shape and the load type, the following three scenarios arise: either only the pull-in instability occurs, or the arch undergoes the snap-through and then the pull-in instability, or the snap-through and the pull-in happen simultaneously. In each case, the pull-in instability occurs.

### 1.3 The dynamic pull-in and snap-through instabilities

The pull-in instability in a MEMS under a transient electric load has been analyzed in [29, 35, 14, 11, 3, 22, 10], and the snap-through of arches and shells during their transient deformations under deformation-independent mechanical loads has been analyzed in [19, 9, 27, 40, 16, 18]. The “dynamic snap-through” generally means a large increase in response resulting from a small increase in a load parameter [19]. Conditions for the dynamic snap-through to occur depend on the geometric parameters of the arch and on the load types. Here we find the arch height  $\hat{h}$  and the load parameter  $\beta$  for which the snap-through instability will occur under a step electric potential difference. We also study different mechanisms of the snap-through instability.

## 2. Mathematical model

The governing equation for a shallow micro-arch under an electrostatic load in terms of non-dimensional variables is [21]

$$\ddot{w} + c\dot{w} + w^{IV} - \alpha(hz_0'' - w'') \int_0^1 (2hz_0' w' - (w')^2) dx = \frac{\beta}{(1 + hz_0 - w)^2}, x \in (0,1) \quad (1)$$

The boundary and initial conditions for a fixed-fixed arch initially at rest are

$$w(0,t) = w(1,t) = w'(0,t) = w'(1,t) = w(x,0) = \dot{w}(x,0) = 0 \quad (2)$$

In equations (1) and (2), a super-imposed dot and a prime denote derivative with respect to time  $t$  and the space coordinate  $x$ , respectively,  $\hat{\epsilon}_0 = 8.854 \times 10^{-12} \text{ Fm}^{-1}$  the vacuum permittivity,  $\hat{\rho}$  the mass density,  $x = \hat{x}/\hat{L}$ ,  $w = \hat{w}/g_0$ , the transverse displacement,  $d = \hat{d}/\hat{g}_0$ ,  $b = \hat{b}/\hat{g}_0$ ,  $h = \hat{h}/\hat{g}_0$ ,  $\alpha = g_0^2 \hat{b} \hat{d} / 2\hat{I}$  the stretch ratio,  $c = \hat{c} \hat{L}^2 / \sqrt{\hat{\rho} \hat{b} \hat{d} \hat{E} \hat{I}}$ ,  $\hat{c}$  the damping coefficient,  $t = \hat{t} \sqrt{(\hat{E} \hat{I}) / (\hat{\rho} \hat{b} \hat{d} \hat{L}^4)}$ ,  $\hat{t}$  the dimensional time,  $\beta = \hat{\epsilon}_0 \hat{b} \hat{L}^4 \hat{V}^2 / 2 \hat{E} \hat{I} \hat{g}_0^3$  the potential difference parameter,  $\hat{\epsilon}_0$  the vacuum permittivity,  $\hat{b}$  the arch width,  $\hat{L}$  the arch length,  $\hat{g}_0$  the initial gap,  $\hat{V}$  the electric potential difference between the two electrodes,  $\hat{E}$  Young's modulus of the arch material,  $\hat{I} = \hat{b} \hat{d}^3 / 12$  the second moment of the cross-section of the arch about its centroidal axis, and  $z_0$  the initial shape of the arch.

As discussed in [10] the damping provided by deformations of the air between the two electrodes can be approximated by the term  $c\dot{w}$ .

We solve equation (1) using the Galerkin method by approximating the transverse displacement  $w$  by the series

$$w(x, t) \approx \sum_{i=1}^n q_i(t) \phi_i(x) \quad (3)$$

where  $q_i(t)$  are the generalized coordinates and  $\phi_i(x)$  eigenmodes of an undamped fixed-fixed straight beam:

$$\phi_i(x) = J_i \left( \frac{\cos(\lambda_i x) - \cosh(\lambda_i x)}{-\sin(\lambda_i) - \sinh(\lambda_i)} - \frac{\sin(\lambda_i x) - \sinh(\lambda_i x)}{\cos(\lambda_i) - \cosh(\lambda_i)} \right) \quad (4)$$

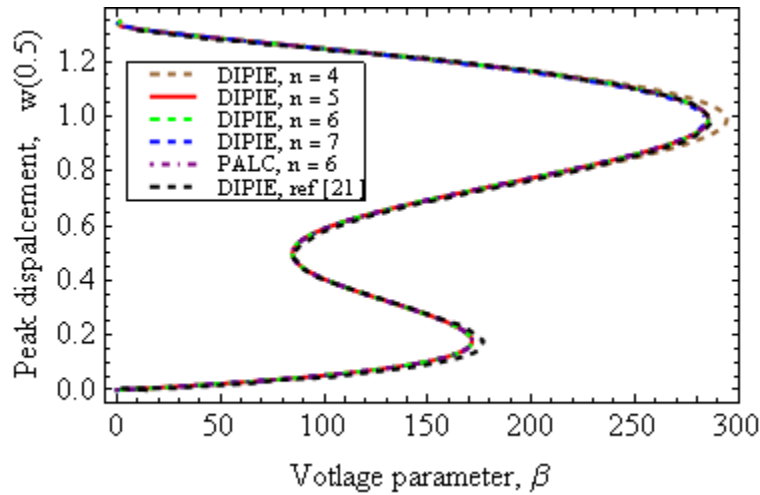


**Figure 2. Bifurcation curve of the peak deflection of the mid-span of the arch versus the applied potential difference parameter for the static problem.**

where  $\lambda_i$  is solution of

$$\cos(\lambda_i) \cosh(\lambda_i) - 1 = 0 \quad (5)$$

The normalization coefficient  $J_i$  is such that  $\max_{0 \leq x \leq 1} (\phi_i(x)) = 1$ , and  $n$  equals the number of modes used in the approximation (3).

Substituting equation (3) into equation (1), multiplying both sides of the resulting equation with  $\phi_i(x)$ , integrating it over the domain (0, 1), integrating by parts terms involving  $w^{IV}$ ,  $z_0''$  and  $w''$ , and using  $\phi(0) = \phi(1) = \phi'(0) = \phi'(1) = 0$  we get

$$\mathbf{M}\ddot{\mathbf{q}} + \mathbf{C}\dot{\mathbf{q}} + \mathbf{B}\mathbf{q} + 2\alpha h^2 \mathbf{z}_0^T \mathbf{q} \mathbf{z}_0 - \alpha h \mathbf{q}^T \mathbf{S} \mathbf{q} \mathbf{z}_0 - 2\alpha h \mathbf{z}_0^T \mathbf{q} \mathbf{S} \mathbf{q} + \alpha \mathbf{q}^T \mathbf{S} \mathbf{q} \mathbf{S} \mathbf{q} = \beta \mathbf{F} \quad (6)$$

where

$$M_{ij} = \int_0^1 \phi_i \phi_j dx \quad (7)$$

$$C_{ij} = c M_{ij} \quad (8)$$

$$B_{ij} = \int_0^1 \phi_i'' \phi_j'' dx \quad (9)$$

$$z_{0i} = \int_0^1 z_0' \phi_i' dx \quad (10)$$

$$S_{ij} = \int_0^1 \phi_i' \phi_j' dx \quad (11)$$

$$F_i = \int_0^1 \frac{\phi_i}{\left(1 + h z_0(x) - \sum_{i=1}^n q_i(t) \phi_i(x)\right)^2} dx \quad (12)$$

Equation (6) is nonlinear in  $\mathbf{q}$  because 5<sup>th</sup>, 6<sup>th</sup> and 7<sup>th</sup> terms on its left-hand side are nonlinear in  $\mathbf{q}$  and the load vector on its right-hand side is a non-linear function of  $\mathbf{q}$ . Boundary conditions in equation (2) are identically satisfied by the assumed form (3) for  $w(x, t)$ . Initial conditions in equation (3) require that  $\mathbf{q}(0) = \mathbf{0}$  and  $\dot{\mathbf{q}} = \mathbf{0}$ . Non-dimensional variables affecting the arch deformation are  $\alpha$ ,  $c$ ,  $h$ ,  $\beta$  and  $z_0'$ .

In subsequent sections, unless stated otherwise, the arch shape is described by  $z_0 = \sin^2(\pi x)$ . Thus, the initial slope of the arch at each clamped end is zero.

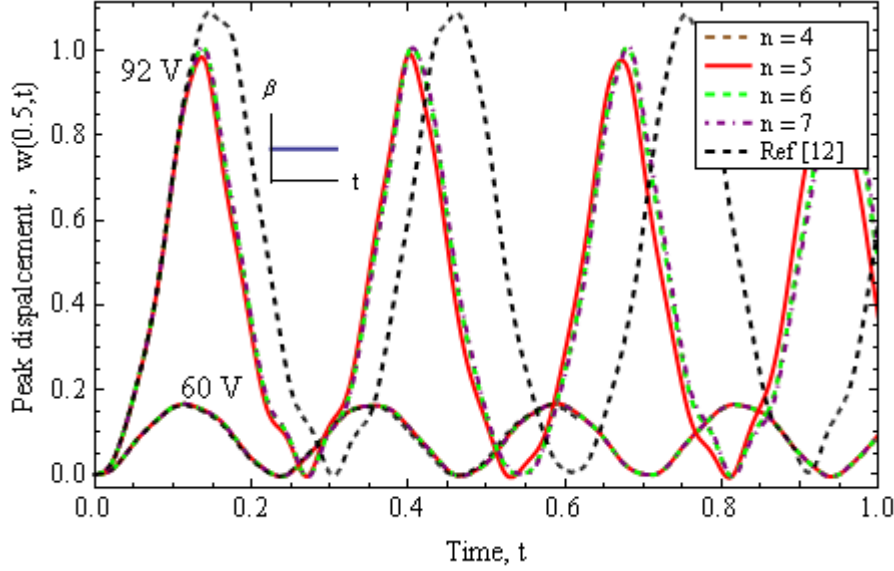


**Figure 3.** Time histories of the peak deflection of the mid-span of the arch due to (a) 60 V ( $\beta = 72$ ) and 92 V ( $\beta = 170$ ) step potential difference between the rigid electrode and the arch.

### 3. Results and discussions

We have developed a computer code to solve equation (6) numerically by writing it in the state space form, and using the software Livermore Solver for Ordinary Differential Equations (LSODE) [36]. The relative and the absolute tolerances in LSODE are set equal to  $10^{-6}$ , and the parameter MF = 22. When solving a static problem we neglect the time dependence of  $\mathbf{q}$  and the first and the second terms on the left-hand side of equation (6), and then solve it using a displacement control approach (displacement iteration pull-in extraction (DIPIE) algorithm [8]) and the pseudo-arc-length continuation (PALC) algorithm [13]. We implement the DIPIE algorithm using the nonlinear equation solver FINDROOT in the commercial computer code MATHEMATICA, and use the freely available software AUTO [1] for the PALC algorithm.

#### 3.1. Validation and Convergence Study

The mathematical model described above has been validated by comparing computed results for four sample problems with those reported in the literature and obtained from a continuum mechanics based approach. First, we consider static deformations of an arch

with  $h = 0.3$  and  $\alpha = 121.5$ . Figure 2 exhibits the bifurcation curve for the arch found with the DIPIE algorithm, the PALC algorithm, and the bifurcation curve for a static problem reported in [21]. Furthermore, results with the PALC and the DIPIE algorithms coincide with each other, and for the DIPIE algorithm the bifurcation curves computed by taking  $n = 5, 6$  and  $7$  in equation (3) are nearly indistinguishable from each other. These results agree very well with those in [21] obtained with the DIPIE algorithm. We also investigated the effect of the number  $n$  of terms in equation (3) upon critical values of  $\beta$  and of the peak displacements at the snap-through and the pull-in instabilities. Critical values of  $\beta$  and of the peak displacements were found to converge as  $n$  increases. For  $n \geq 6$ , the change in the critical values of  $\beta$  and the peak displacements at the two instabilities is less than 1%. Unless noted otherwise, results presented below are  $n = 6$  in equation (3). Arches studied herein have only one stable shape, namely the initial shape, when the power is lost ( $\beta = 0$ ). However, for a range of values of  $\beta$  (e.g.,  $70 < \beta < 170$  see figure 2) the arch has two stable equilibrium positions for the same value of  $\beta$ .

Referring to figure 1, we consider a bell shaped silicon arch with  $\hat{L} = 1$  mm,  $\hat{b} = 30$   $\mu\text{m}$ ,  $\hat{d} = 2.4$   $\mu\text{m}$ ,  $\hat{g}_0 = 10.1$   $\mu\text{m}$ ,  $\hat{h} = 3.0$   $\mu\text{m}$ , and its bottom-surface described by  $z_0 = \sin^2(\pi x / \hat{L})$ . Values assigned to material parameters are  $\tilde{E} = 169$  GPa and Poisson's ratio  $\nu = 0.3$ . We analyze it as a plane strain problem by using the effective Young's modulus  $\hat{E} = \tilde{E} / (1 - \nu^2)$ , and account for fringing fields by increasing the Coulomb pressure  $F_i$  (cf. equation (12)) according to the Mejis-Fokkema formula [6, 21]:

$$F_i = \int_0^1 \frac{\phi_i}{(1 + h z_0(x) - w(x))^2} F_g dx \quad (13)$$

where

$$F_g = \left( 1 + 0.265 \left( \frac{1 + z_0(x) - w(x)}{b} \right)^{3/4} + 0.53 \left( \frac{d}{b} \sqrt{\frac{1 + z_0(x) - w(x)}{d}} \right) \right) \quad (14)$$



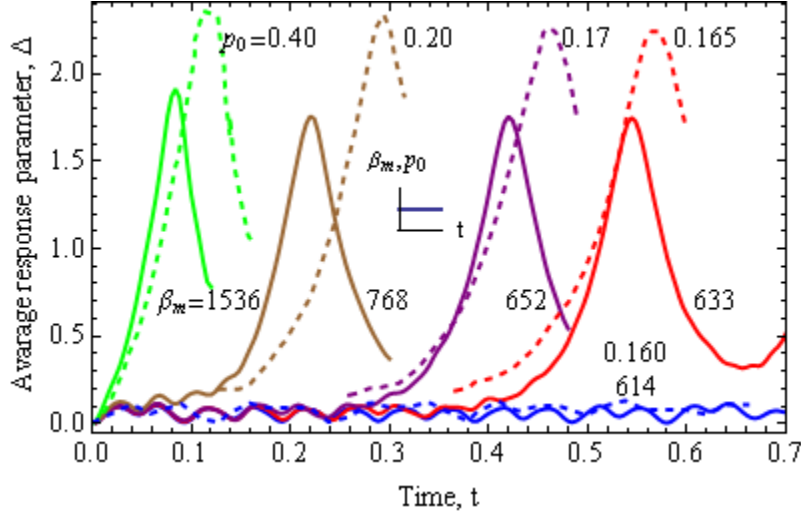


**Figure 4.** Time histories of the average response parameter for the circular arch ( $h = 1.0$ ) for different values of  $\beta_m = \left(\hat{d}^2 \hat{L}^2 \hat{b} / \hat{R}^2 \hat{I} \hat{h}\right) p_0$ . Although, value of  $\beta_m$  is different from  $p_0$  in the figure, they represent the same load. Solid curves are computed from the present model, dashed curves are from [19].

For different number of terms in equation (3), figure 3 shows the peak displacement  $w(0.5, t)$  versus time  $t$  for 60 V and 92 V step potential differences and those reported in [12]. Time histories of the peak displacement for 60 V step electric potential difference agree well with those reported in [12]. However, for 92 V potential difference, the maximum peak displacement and the time period of oscillation are 8% and 20% lower, respectively, than those reported in [12]. In [12], the problem is analyzed using the coupled finite element and boundary element methods assuming that the arch is in plane strain state of deformation, the electric load is computed after every time step accounting for deformations of the arch, and the electric load is applied normal to the deformed surface of the arch. Here the Coulomb pressure is found by using the parallel plate approximation (PPA) [7] and it acts vertically downwards. The effect of the arch curvature on the Coulomb pressure increases as the arch comes close to the bottom electrode. In section 3.5, a detailed comparison of results from the present method with those from the continuum mechanics based approach is given.

As results for the dynamic and the static problems found using  $n = 5, 6,$  and  $7$  are virtually the same, henceforth we take  $n = 6$ .

We now compare results for a dynamic snap-through instability of a shallow circular arch with geometric imperfection (initial shape of the arch  $z_0 = (4-4x)x + 0.01d \sum_{i=2,4,6} \phi_i(x)$ ) under a mechanical pressure load with those reported in [19]. Equation (6) governs deformations of an arch under a mechanical pressure load if the potential difference parameter  $\beta$  is replaced by a load parameter  $\beta_m$  and the generalized force  $F_i$  (cf. equation (12)) by  $F_i = \int_0^1 \phi_i dx$ . We use  $\hat{h}$  in place of  $\hat{g}_0$  to non-dimensionalize the deflection  $\hat{w}$  and the arch thickness  $\hat{d}$ . A different non-dimensional load parameter  $p_0 = \beta_m / (\hat{d}^2 \hat{L}^2 \hat{b} / \hat{R}^2 \hat{I} \hat{h})$  is used in [19].  $\hat{R}$  is the radius of the circular arch.

Figure 4 exhibits time histories of the average response parameter

$$\Delta(t) = \int_0^1 w(x, t) dx / \int_0^1 z_0(x) dx \text{ for the arch } (h = 1.0, \alpha = 150) \text{ for different values of } \beta_m. \text{ A}$$

large change in the response of the arch is observed when  $\beta_m$  is increased from 614 ( $p_0 = 0.159$ ) to 615 ( $p_0 = 0.160$ ). Therefore, the load  $\beta_m$  for the snap-through instability is between 614 and 615. In [19], this load is reported to be between  $p_0 = 0.160$  ( $\beta_m = 615$ ) and  $p_0 = 0.165$  ( $\beta_m = 633$ ). However, the maximum value of the average response parameter  $\Delta$  for  $p_0 = 0.165$  ( $\beta_m = 633$ ) from the present work is 21.5% lower than that reported in [19]. In [19], equation (6) is solved using an analog computer system with servo-multipliers providing the nonlinear terms. The solutions of frequency equation (5) and the mode shapes (cf. equation 4) are approximated such that values of different terms in equations (7) to (12) are accurate only to three significant digits. Here, we have used LSODE with the double precision arithmetic. We note that the presently computed response of the arch agrees qualitatively with that given in [19] and the two values of the load for the snap-through instability agree well with each other.

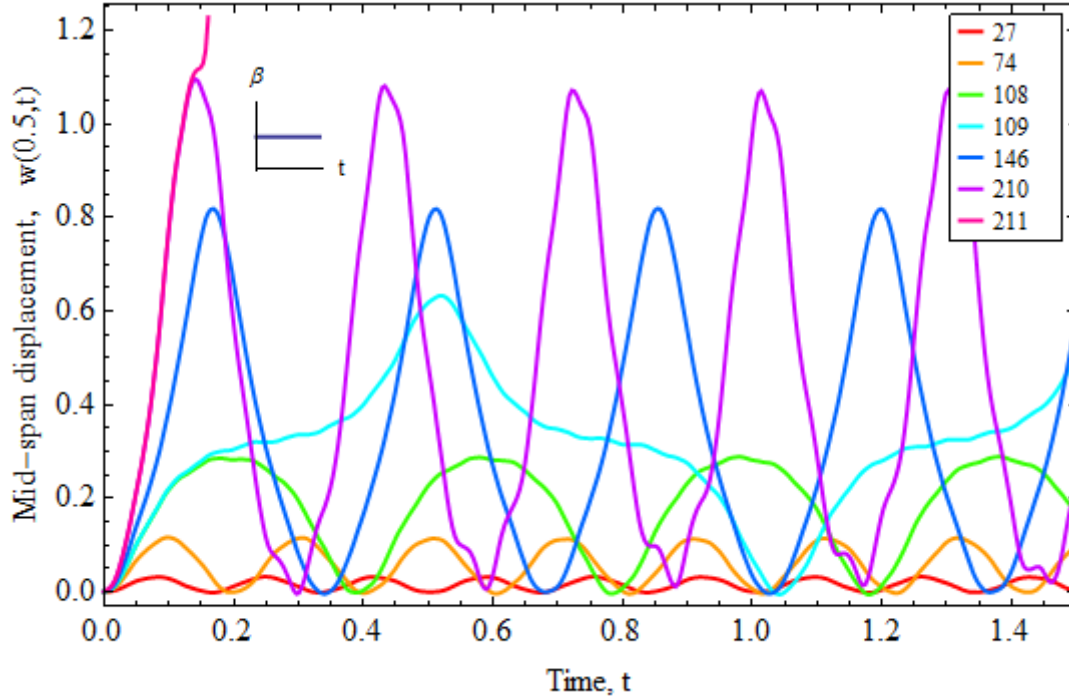


**Figure 5. Time histories of the downward displacement of the mid-span of the fixed-fixed bell shaped arch ( $h = 0.3$ ) for different values of  $\beta$ .**

### 3.2. Direct snap-through instability

For a bell shaped silicon arch with  $\alpha = 110$ ,  $h = 0.3$ ,  $z_0(x) = \sin^2(\pi x)$ , figure 5 shows time histories of the mid-span deflection for different values of the applied step potential difference. A significant difference in the response of the arch occurs when  $\beta$  is increased from 108 to 109 in that the amplitude and the time period of oscillation increase noticeably. This sudden change in the response due to a small change in  $\beta$  indicates the snap-through instability. The critical value of  $\beta$  is between 108 and 109. By solving the problem for several values of  $\beta$  between 108 and 109 (e.g. obtained by the bisection method), one can compute a better value of  $\beta$  for the snap-through instability. The critical value of  $\beta$  for the pull-in instability is found to be between 210 and 211, since for  $\beta = 210$  the response of the arch remains bounded but for  $\beta = 211$  it becomes unbounded.

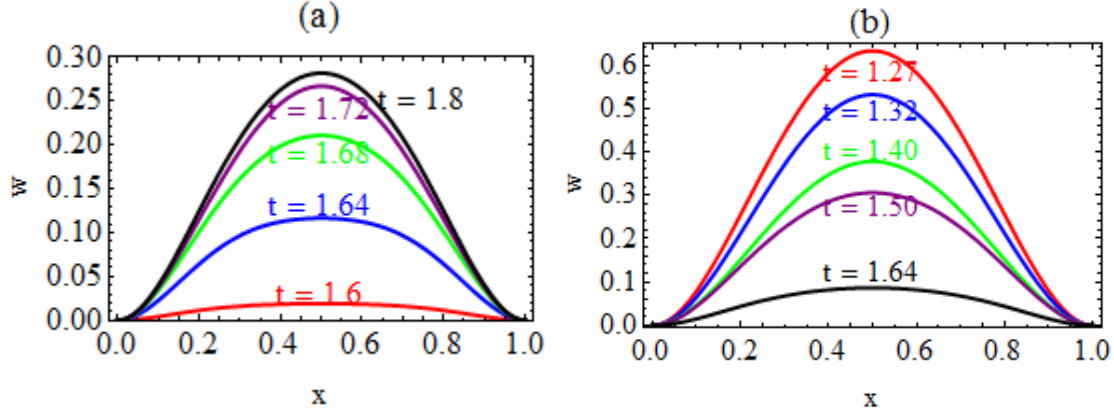


Figure 6. Snap shots of the displacement of the arch ( $h = 0.3$ ) for (a)  $\beta = 108$  and (b)  $\beta = 109$

Figure 6 shows, at different times, snap shots of the deformed arch for  $\beta = 108$  (before the snap-through) and 109 (after the snap-through). It is clear that both before and after the snap-through the arch deforms symmetrically about the plane  $x = 0.5$ . Time histories of the generalized coordinates for  $\beta = 108$  and 109, not included here, evinced that participations of the asymmetric modes with coefficients  $q_2$ ,  $q_4$  and  $q_6$  are negligible as compared to those of the symmetric modes with coefficients  $q_1$ ,  $q_3$  and  $q_5$ . It is clear that a reasonably accurate response of the arch can be computed by considering only the fundamental mode in equation (3).

For several values of the arch height, figure 7 depicts loci of the maximum deflection produced by different step electric potentials, and static bifurcation curves obtained by using the DIPIE and the PALC algorithms. In every case, the bifurcation curve obtained from the DIPIE algorithm coincides with that obtained from the PALC algorithm. We note that the snap-through due to a step electric potential difference occurs when the locus of the maximum deflection intersects the unstable branch of the static bifurcation curve (e.g., point D for  $h = 0.3$  and  $0.35$  in figures 7a and 7b). A similar observation is reported in [27] due to a displacement-independent mechanical pressure load wherein the snap-through is called the ‘direct snap-through’ because the external pressure directly induces snapping of the symmetric mode in contrast to the ‘indirect snapping’ induced due to the parametric excitation of asymmetric modes as reported in the next section.

We note that after the snap-through instability (e.g., point D) arch's deformations are stable (e.g., point K) and the locus of the maximum displacement continues along the path KL until it again intersects the unstable branch of the static bifurcation curve (e.g., point L) when the pull-in instability occurs.

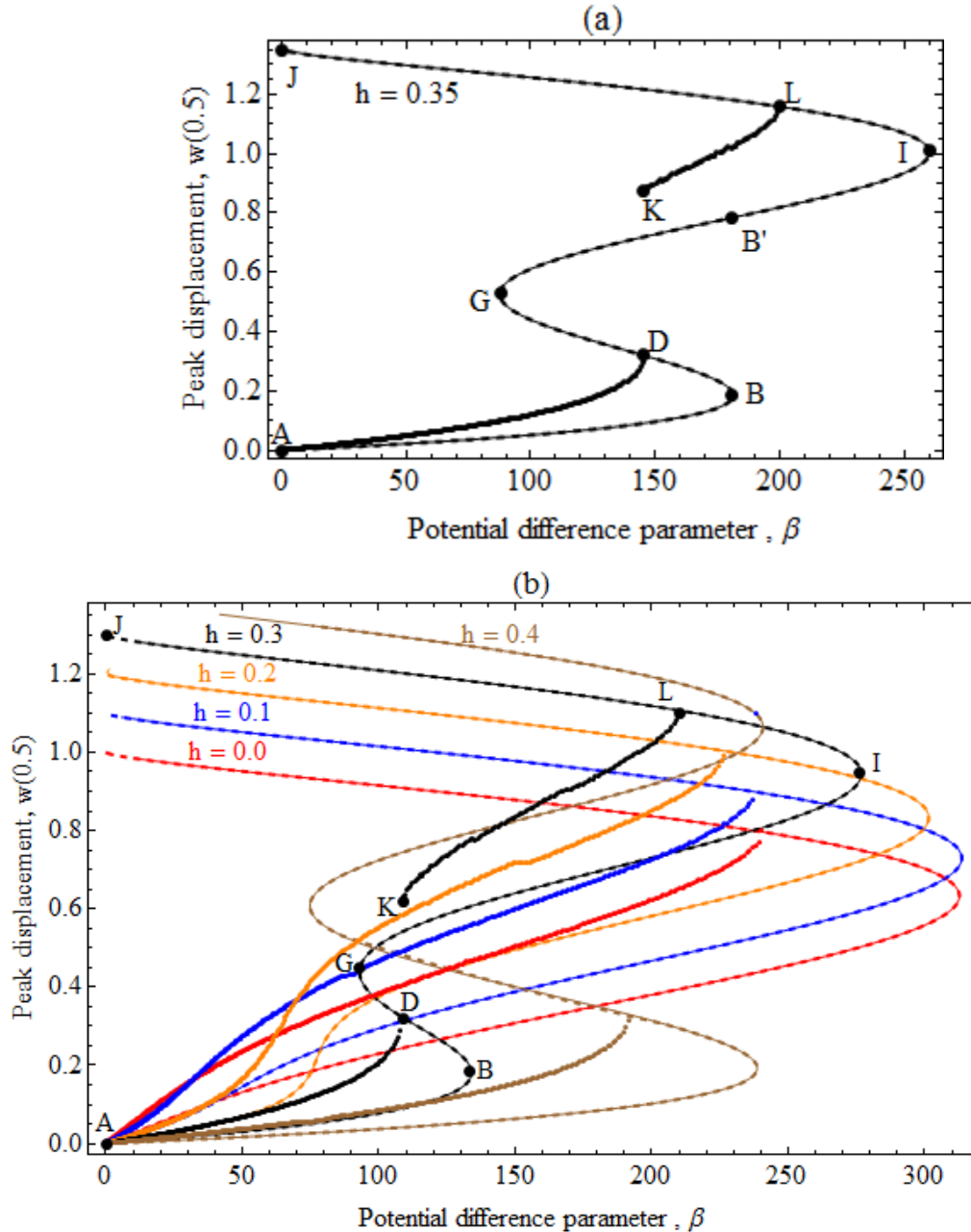
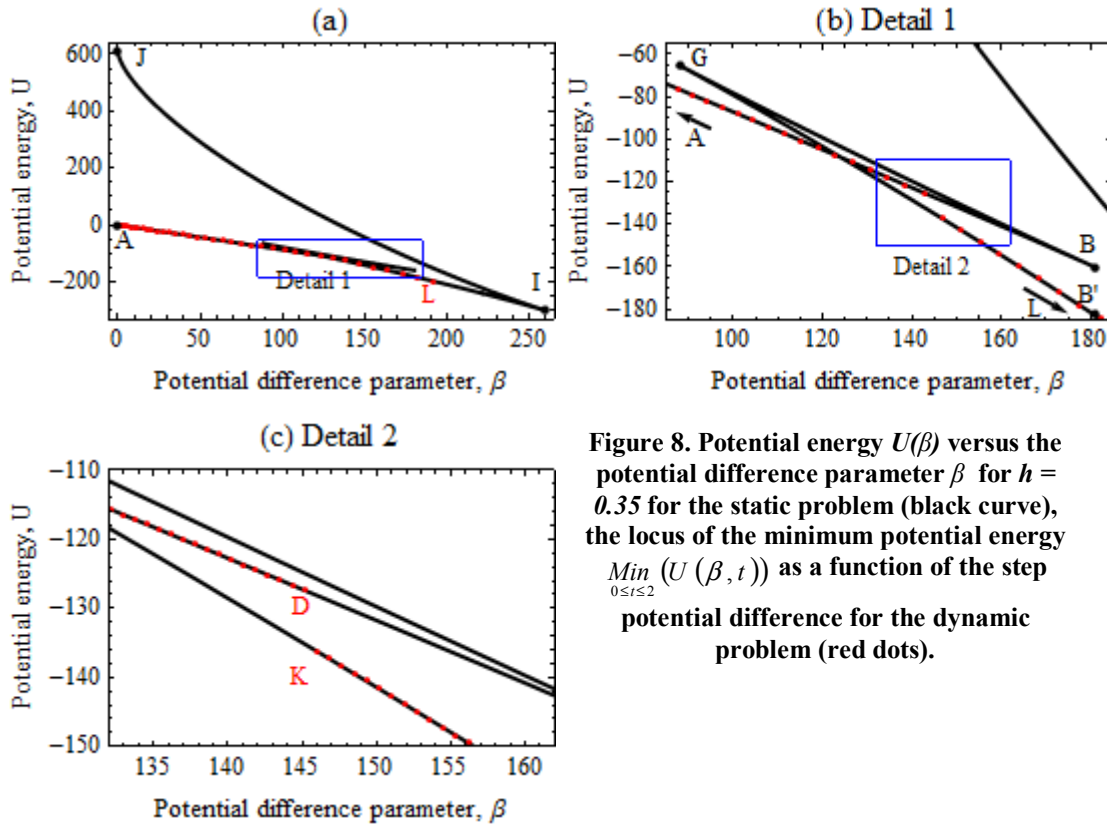


Figure 7. Bifurcation diagrams ( $w(0.5)$  vs.  $\beta$ ) of the arch for different arch heights for static problems. Dashed curves and light solid curves are results from the DIPE and the PALC algorithms, respectively. Dark solid curves are the loci of the maximum displacement  $\text{Max}_{0 \leq t \leq 2} (w(0.5, t))$  under a step potential difference. Results from the DIPE and the PALC algorithms overlap each other. Figure 7(a) for  $h = 0.35$  clearly shows different curves.

For  $h = 0.0$  and  $0.2$ , there is no snap-through instability, and the locus of the maximum deflection continues until the pull-in instability ensues. Therefore, a minimum height is required for the arch to undergo the snap-through instability; e.g. see section 3.4. For  $h = 0.4$  no stable configuration under a step electric potential difference is observed after the snap-through instability as the pull-in instability occurs immediately.



**Figure 8. Potential energy  $U(\beta)$  versus the potential difference parameter  $\beta$  for  $h = 0.35$  for the static problem (black curve), the locus of the minimum potential energy  $\text{Min}_{0 \leq t \leq 2} (U(\beta, t))$  as a function of the step potential difference for the dynamic problem (red dots).**

At the snap-through instability for  $h = 0.3$  and the step potential difference,  $\beta$  is  $\sim 15\%$  less and the peak displacement  $w$  is  $\sim 50\%$  more than their values for the corresponding static problem. At the pull-in instability,  $\beta$  is  $\sim 22\%$  less and the peak displacement  $\sim 21\%$  more than those for the static problem. Thus, the snap-through and the pull-in voltages for the dynamic problem are less than those for the static problem, but the snap-through and the pull-in deflections for the dynamic problem are greater than those for the static problem.

Figure 8 exhibits the variation of the potential energy versus  $\beta$  for a static problem with  $h = 0.35$  and  $\alpha = 110$ . The non-dimensional potential energy  $U$  is given by [21]

$$U = \frac{1}{2} \int_0^1 (w'')^2 dx + \frac{\alpha}{4} \left\{ \int_0^1 (2hz_0' w' - (w')^2) dx \right\}^2 - \beta \int_0^1 \frac{dx}{(1 + hz_0 - w)} \quad (15)$$

For a dynamic problem with  $\beta$  a step function of time,  $w$  and  $U$  are functions of time. In figure 8, we also plot as red dots the locus of the minimum values of  $U$  for given step values of  $\beta$ . Points A, B, D etc. in figure 8 are for the same values of  $\beta$  as those in figure 7(a). For a static problem,  $U$  decreases from point A to point B as the value of  $\beta$  increases. At point B, the arch experiences the snap-through instability and the value of  $U$  suddenly drops from -160 corresponding to point B to -182 for point B' (see figure 8(b)). After the snap-through,  $U$  gradually decreases from -182 at point B' to -301 at point I when the pull-in instability happens. For the dynamic problem, the locus of the minimum potential energy (red dots in figure 8) follows the curve of  $U$  versus  $\beta$  for the static problem from point A to point D. At point D, with a small increase in  $\beta$ , the minimum potential energy drops from -130 at point D to -138 at point K, this indicates the snap-through instability. For the static problem, the locus of the minimum potential energy follows the curve of  $U$  versus  $\beta$  from point K to point L where the pull-in instability happens (figure 8(a)).

### 3.3. Indirect snap-through instability

For arch height  $h = 0.5$ , figure 9 shows time histories of the mid-span deflection of the arch for different values of the step potential differences  $\beta$ . At  $\beta = 293$  the arch undergoes several cycles of moderate-amplitude oscillations before snapping. The pull-in instability occurs immediately after the snap-through instability. The critical value of  $\beta$  is between 292 and 293. This behavior is significantly different from that observed for  $h = 0.3$  and  $h = 0.35$  for which the snap-through instability ensued without the arch undergoing oscillations.

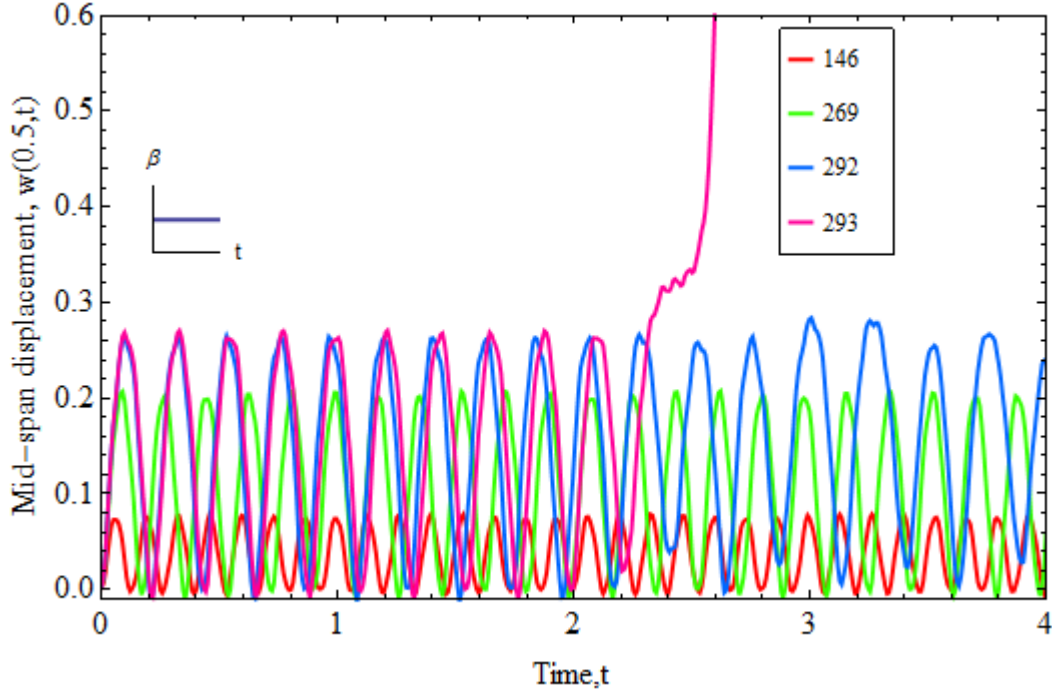


Figure 9. For different applied step voltages time histories of the downward displacement of the mid-span of the fixed-fixed bell shaped arch with  $h = 0.5$ .

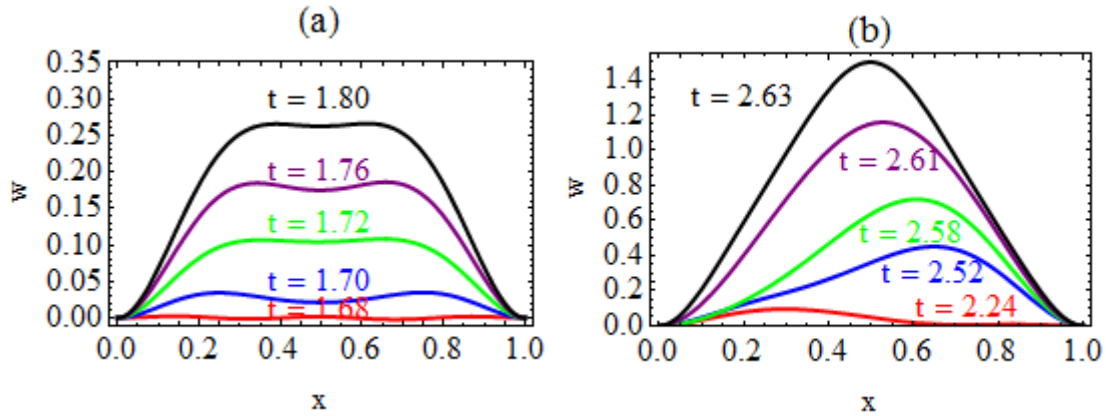


Figure 10. Snap shots of the displacement of the arch ( $h = 0.5$ ) for (a)  $\beta = 292$  and (b)  $\beta = 293$ .

Figure 10 exhibits the deformed arch at different non-dimensional times for  $\beta = 292$  (before the snap-through) and 293 (after the snap-through). It is clear that the arch deforms symmetrically about  $x = 0.5$  before the snap-through instability but asymmetrically after the snap-through. However, we observe that just before the arch touches the bottom electrode at  $t = 2.63$ , its deflections are again symmetric about  $x = 0.5$ . Figure 11 exhibits time histories of the generalized coordinates for  $\beta = 292$  and 293.



These evince that the participation of the asymmetric modes ( $q_2$ ,  $q_4$  and  $q_6$ ) grows considerably after  $t = 2.2$  when the snap-through instability occurs. Whereas values of  $q_2$ ,  $q_4$  and  $q_6$  for the snap-through instability discussed in section 3.2 were of the order of  $10^{11}$ , those in figure 11 are of the order of  $10^{-1}$ ,  $10^{-2}$  and  $10^{-3}$  respectively. Asymmetric modes do start to participate in deformation of the arch for  $\beta = 292$  after  $t = 2.2$ . However, participations of the asymmetric modes remain bounded and do not cause either the snap-through or the pull-in instability. On the other hand, for  $\beta = 293$ , the displacement of the arch becomes unbounded at about  $t = 2.2$  and the pull-in instability occurs. These suggest that the participation of mode 2 is more than that of modes 4 and 6 in making deformations of the arch asymmetric about  $x = 0.5$ .

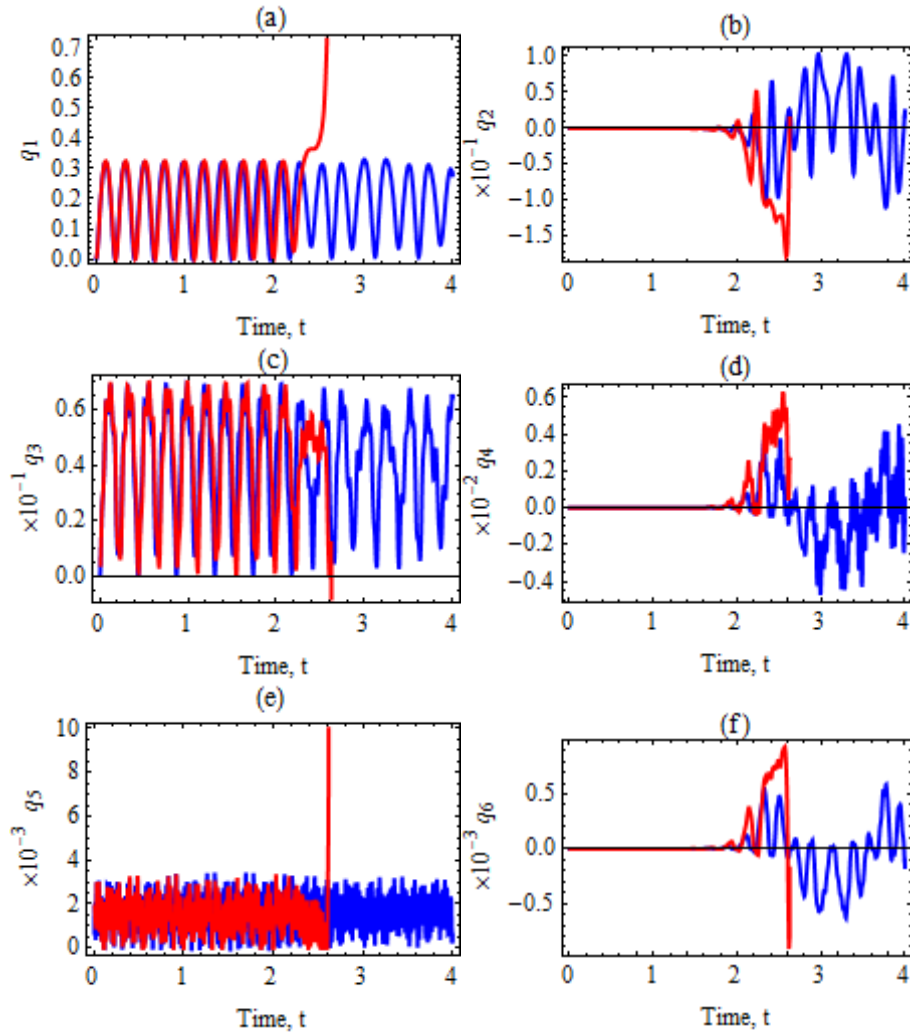


Figure 11. Time histories of  $q_1, q_2 \dots q_6$  for  $\beta = 292$  (blue curves) and  $\beta = 293$  (red curves).

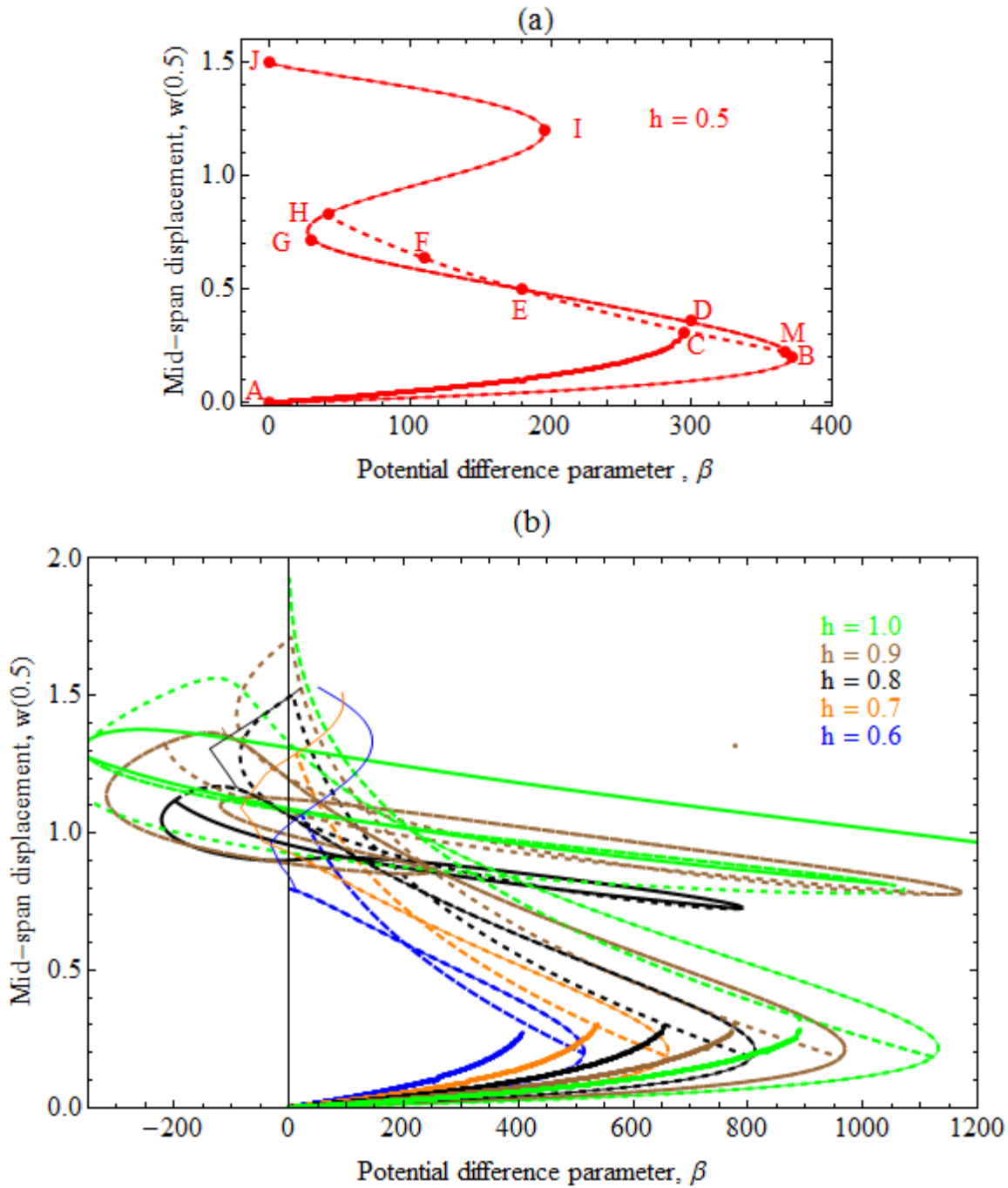


Figure 12. Bifurcation diagrams ( $w(0.5)$  vs.  $\beta$ ) of the arch for different arch heights for static problems. Dashed curves and light solid curve are results from the DIPIE and the PALC algorithms, respectively. Dark solid curves are the loci of the maximum displacements  $\text{Max}_{0 \leq t \leq 4} (w(0.5, t))$  under the step load. Results of the DIPIE and the PALC algorithms overlap only when arch's deformations are symmetric about  $x = 0.5$ .

The reason of the snap-through instability with asymmetric deformations is the parametric excitation of the anti-symmetric modes arising through coupling terms such as  $q_i q_{i+1}$  (with  $i = 1 \dots n-1$ ) in equation (6). These terms act as an effective load whose magnitude increases as the amplitude of the anti-symmetric motion grows under the parametric excitation. If the amplitude of anti-symmetric motion becomes sufficiently large, a critical effective load is reached, and the snap-through instability occurs. This second kind of snapping is called ‘indirect snap-through’ or ‘parametrically induced snap-through’ in [27] where snapping of a shallow arch under a displacement-independent step pressure load is studied. Note that for the electric loading  $F_i$  in equation (6) also depends on deformations of the arch, unlike for the displacement-independent pressure load where  $F_i$  is independent of  $q_i$ ; thus, there are more coupled terms in the MEMS problem than those in the mechanical problem analyzed in [27]. Results for a problem reported in the next section show that under an electric load an arch is more prone to snap through asymmetrically than under displacement-independent mechanical loads.

Figure 12 depicts loci of the maximum deflection produced by a step electric potential for the transient problem, and bifurcation curves for static problems obtained with the DIPIE and the PALC algorithms for  $h = 0.5, 0.6, 0.7, 0.8, 0.9$ , and  $1.0$ . In every case, the bifurcation curve for symmetric deformations computed with the DIPIE algorithm overlaps that obtained with the PALC algorithm (e.g., the curve ABMDEGHIJ for  $h = 0.5$  in figure 12(a)). The DIPIE algorithm does not give asymmetric solutions [5, 33] (e.g., the dashed curve MCEF H for  $h = 0.5$  in figure 12(a)), which are obtained by the PALC algorithm. We note that, for all values of  $h$ , the snap-through due to the step load occurs when the locus of the maximum deflection intersects the unstable branch of the static bifurcation curve (e.g., point C for  $h = 0.5$  in figure 12(a)) corresponding to the asymmetric solution. The pull-in instability happens immediately after the snap-through instability. Values of  $\beta$  and the peak deflection  $w$  at the snap-through instability due to a step potential difference (e.g., point C for  $h = 0.5$ ) for the dynamic problem are  $\sim 20\%$  lower and  $\sim 25\%$  higher, respectively, than those for the corresponding static problem (e.g., point B for  $h = 0.5$ ). For  $h \geq 0.8$ , complex branches of the bifurcation diagram

corresponding to unstable deformations of the arch are found from the PALC algorithm. A similar behavior, known as the looping behavior of an arch, is reported in [15, 45] due to displacement-independent mechanical pressure load. Results in figure 12b for  $\beta < 0$  are not valid because  $\beta$  cannot be negative. For asymmetric deformations of the arch corresponding to a point on the dashed curve BCEFH for  $h = 0.5$  in figure 12(a) the PALC algorithm gives two solutions displayed in figure 13.

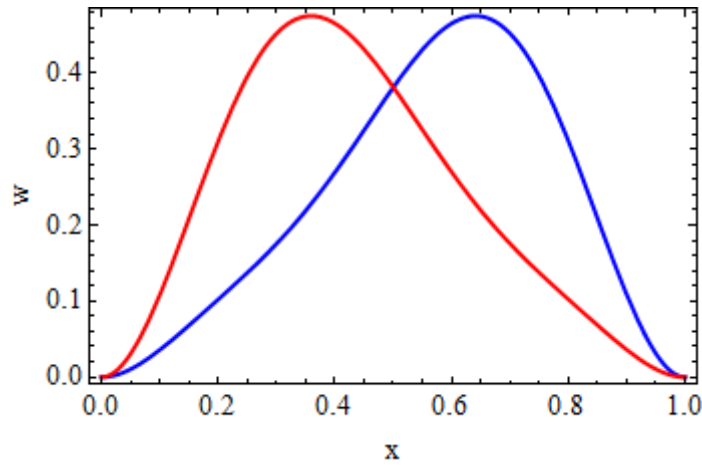


Figure 13. The two asymmetric solutions for  $h = 0.5$  and  $\beta = 250$ .

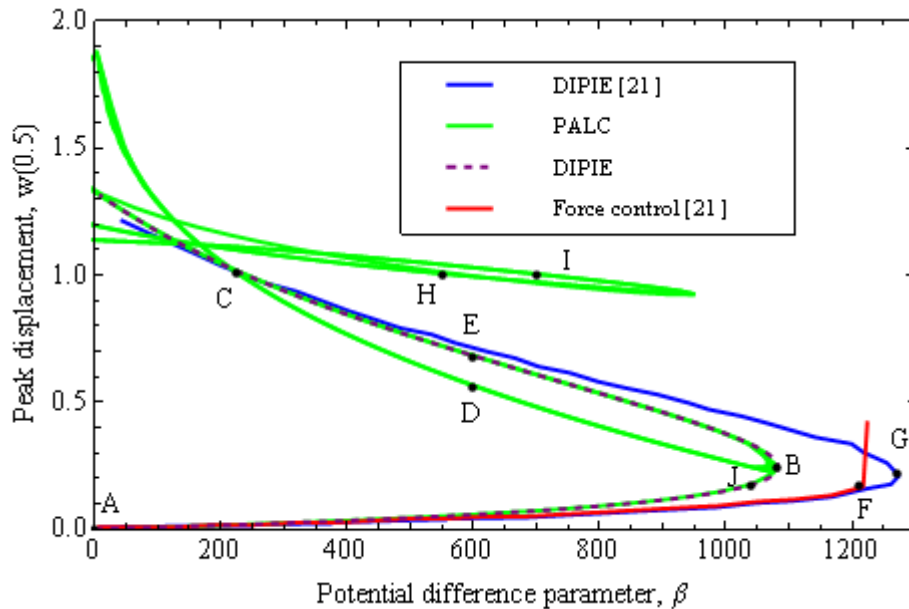
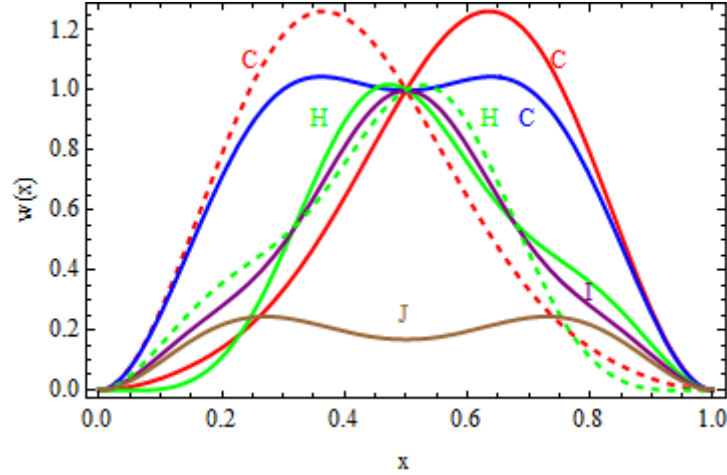


Figure 14. Bifurcation diagrams ( $w(0.5)$  vs.  $\beta$ ) of the arch for different arch heights for static problems ( $h = 0.5, \alpha = 250$ ).



**Figure 15. Deformations at different points of the bifurcation diagram for  $h = 1.0$  and  $\alpha = 110$ .**

In [21], the symmetry breaking of arches under electric loads in static problems is studied using a force control method and taking  $n = 15$  in equation (3). Figure 14 compares the presently computed bifurcation curve for an arch with  $h = 0.5, \alpha = 250$  and  $n = 6$  with that reported in [21]. The bifurcation curve (ABEC from our code and AFGEC from [21]) computed with the DIPIE algorithm fails to show asymmetric deformations of the arch. Asymmetric deformations (BDC) and the looping behavior are observed in the solution from the PALC algorithm. In [21], the symmetry breaking is found with the force control method. The critical value of  $\beta$  at the snap-through instability computed with our code is 16.7% less than that reported in [21]. We found that increasing  $n$  from 6 to 10 does not change results appreciably and including mode shapes for  $n > 10$  increases numerical inaccuracies because for large  $\lambda_i$   $\cos(\lambda_i x)$  is very small as compared to values of  $\sinh(\lambda_i x)$  and  $\cosh(\lambda_i x)$ . Present computations also show looping behavior of the arch; however, these curves (e.g. marked H and I) correspond to unstable equilibrium shapes of the arch.

Figure 15 exhibits several unstable and one stable solution for the arch corresponding to different points on the bifurcation curve in figure 14. Deformations corresponding to points C, H and I are unstable, which means the arch may have those equilibrium configurations under a static load of  $\beta = \sim 230, \sim 550$  and  $\sim 700$ , respectively. However, a small perturbation will cause the arch to experience the pull-in instability. Points C and H represent multiple symmetric and asymmetric deformations of the arch.

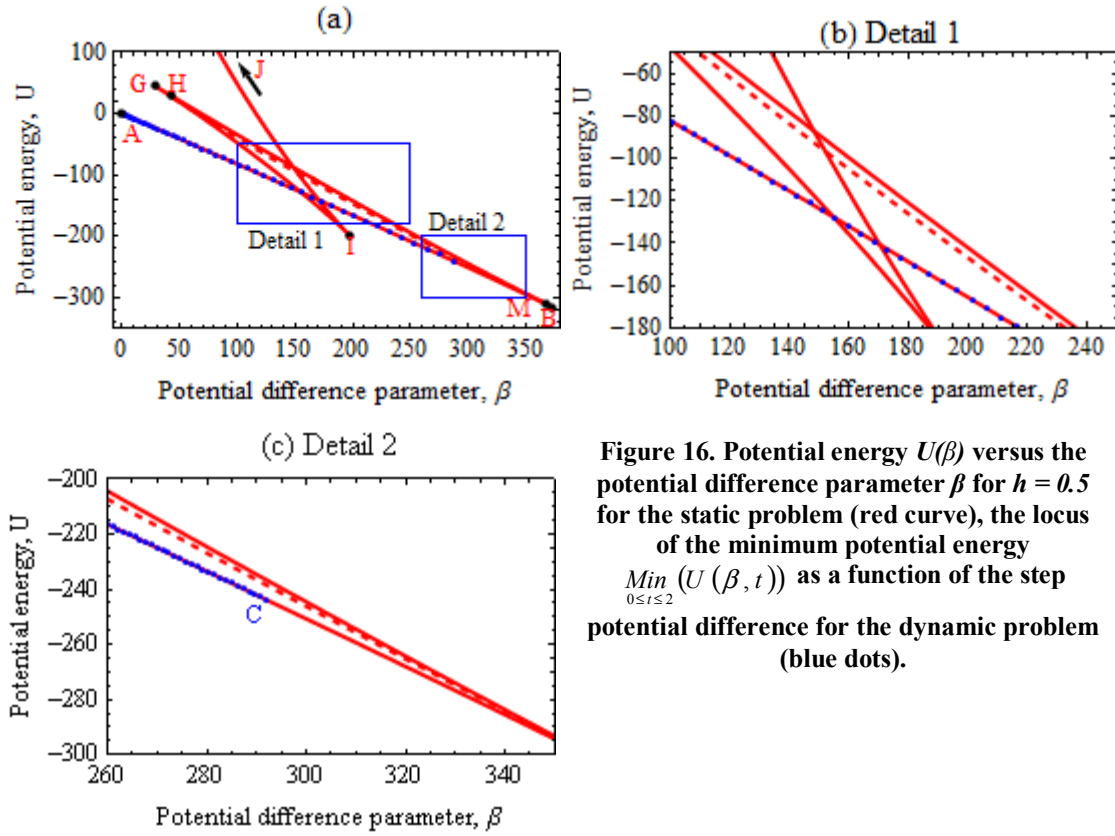


**Figure 16. Potential energy  $U(\beta)$  versus the potential difference parameter  $\beta$  for  $h = 0.5$  for the static problem (red curve), the locus of the minimum potential energy  $\text{Min}_{0 \leq t \leq 2} (U(\beta, t))$  as a function of the step potential difference for the dynamic problem (blue dots).**

Figure 16 exhibits the variation of  $U$  versus  $\beta$  for a static problem with  $h = 0.5$  and  $\alpha = 110$ . In figure 16, we have also plotted for transient problems the locus of the minimum values of  $U$  for step voltages  $\beta$ . Points A, B, C, etc. in figure 16 have the same values of  $\beta$  as those in figure 12(a). For a static problem,  $U$  decreases from 0 at point A to  $\sim -300$  at point B as  $\beta$  increases from 0 to 370. We note that there is no other solution with lower value of  $U$  than that at point B. At point B, the arch experiences the snap-through instability followed immediately by the pull-in instability and no solution exists for a value of  $\beta$  that is higher than the value of  $\beta$  at point B. We also note that for  $h = 0.35$  (see figure 11), the value of  $\beta$  at point I is higher than the value of  $\beta$  at point B, whereas for  $h = 0.5$  (see figure 16), the value of  $\beta$  at point I is lower than that at point B. In figure 16(b), the total potential energy for an unstable asymmetric solution corresponding to a point on the dashed curve MH is lower than that for the unstable symmetric solutions represented by the solid curve BH. The locus of the minimum potential energy for the dynamic problem denoted by blue dots in figure 16 follows the curve of  $U$  versus  $\beta$  for

the static problem from point A to point C. At point C, the snap-through instability and the pull-in instability happen simultaneously for the dynamic problem.

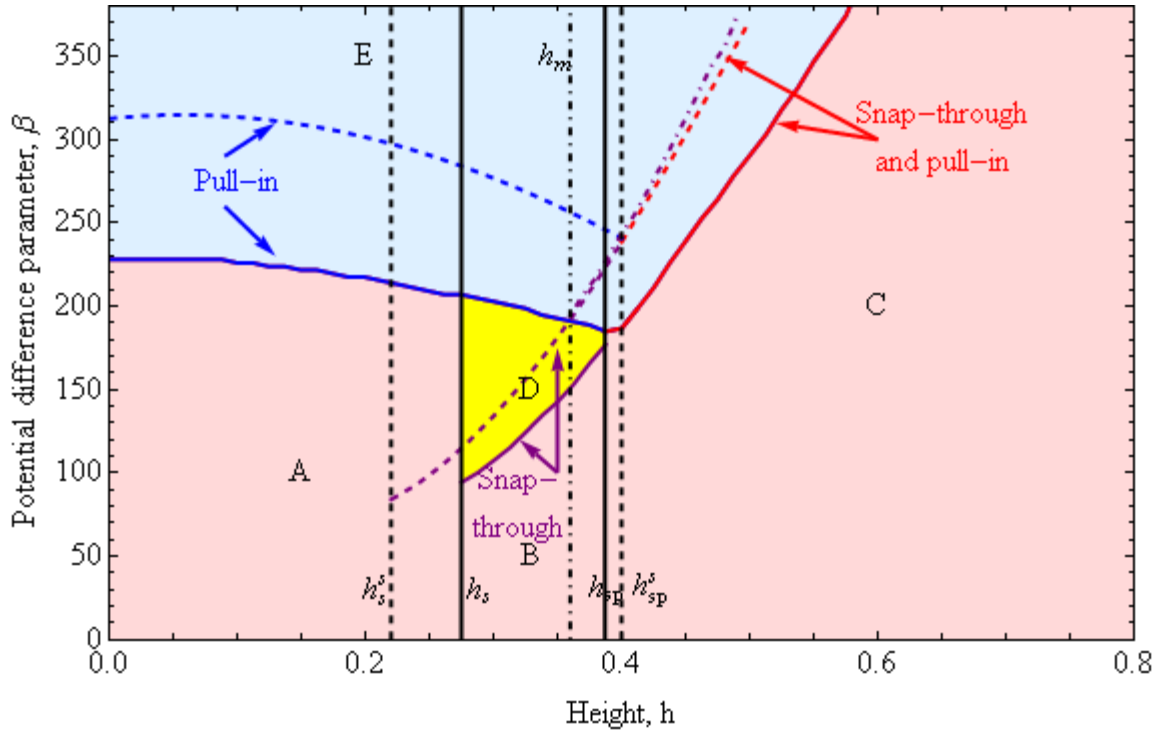


**Figure 17.** Critical values of  $\beta$  for the snap-through (purple curve) and the pull-in instabilities (blue curve) to occur for an arch with  $\alpha = 106.0$ . The red curve shows critical values of  $\beta$  for which the snap-through and the pull-in instabilities occur simultaneously. Solid and dashed curves correspond, respectively, to results for the dynamic and the static problems. The dot dashed curve represents results for the dynamic problem with a displacement-independent load.

### 3.4. Comparison of results for dynamic problems with those for static problems

The critical potential difference parameters for the pull-in instability (blue curve), the snap-through instability (purple curve), and the snap-through followed immediately by the pull-in instability (red curve) are plotted as function of the arch height in figure 17 for  $\alpha = 106.0$ . Solid and dashed curves correspond, respectively, to results for dynamic and static problems due to the application of the step electric potential difference. Note that only value of  $h$  and  $\beta$  are varied and other parameters for the MEMS are kept unchanged. For  $h$  between  $0.0$  and  $0.8$ , the critical values of  $\beta$  for dynamic problems are ‘substatic’ in the sense that they are lower than those for the corresponding static problems. The minimum height  $h_s^s = 0.22$  required for the arch to experience the snap-through

instability for a static problem is less than the corresponding value of  $h_s = 0.275$  for the dynamic problem. However, the minimum arch heights at which the blue and the purple curves meet each other are almost the same for the static and the dynamic problems (e.g.,  $h_{sp}^s = 0.4$ ,  $h_{sp} = 0.37$ ). An arch with a height greater than  $h_{sp}$  will experience the pull-in instability immediately after the snap-through instability under a step electric potential difference;  $h_{sp}^s$  is the corresponding value for the static problem. The dot-dashed purple curve shows critical values of  $\beta$  for the snap-through instability due to a step displacement-independent mechanical load given by equation (15).

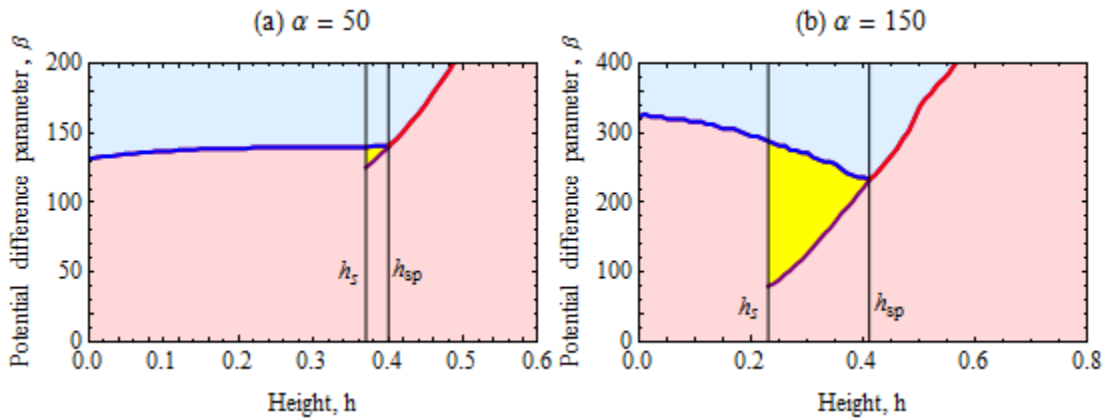


**Figure 18.** Critical values of  $\beta$  for the snap-through (purple curve) and the pull-in instabilities (blue curve) to occur for an arch with (a)  $\alpha = 50.0$  and (b)  $\alpha = 150.0$ . The red curve shows the critical values of  $\beta$  for which the snap-through and the pull-in instabilities occur simultaneously.

The minimum arch height  $h_m$  required for the snap-through instability to occur for this mechanical load is greater than  $h_s$  for the displacement-dependent step electric load. Therefore, arches under electric loads are more prone to the snap-through instability, and results from studies of the response of an arch for a displacement-independent load cannot be directly used to predict the response of the same arch under an electric load.

The curves of critical values of  $\beta$  for step electric loads divide the plot of  $\beta$  vs.  $h$  in figure 17 into three regions. An arch of height  $h$  under a potential difference  $\beta$  from regions A, B and C (light red) will experience oscillations of relatively small amplitude and time period without experiencing a snap-through instability. On the other hand, an arch of height  $h$  under a potential difference  $\beta$  from region D (yellow) will experience oscillations of large amplitude and large time period after undergoing the snap-through.



However, an arch under a potential difference  $\beta$  from region E (light blue) will not have any stable motion; it will experience the pull-in instability and will touch the bottom electrode.

Figure 18 exhibits plots of  $\beta$  vs.  $h$  for dynamic problems and two values, 50 and 150, of  $\alpha$ . Results in figure 18 for the two values of  $\alpha$  are quantitatively different but are qualitatively similar to those for  $\alpha = 106$  in figure 17. For different values of  $\alpha$ , table 1 lists values of the minimum heights  $h_s$  and  $h_{sp}$  required for the snap-through and the combined snap-through and pull-in instabilities, respectively. The value of  $h_s$  decreases with an increase in the value of  $\alpha$ , however, that of  $h_{sp}$  remains the same. The size of the yellow region increases with an increase in the value of  $\alpha$ . For small values of  $\alpha$ , this region will vanish. Figures 17 and 18 provide a qualitative idea of the phase diagram of a micro-arch under a step electric load and give quantitative information for  $\alpha = 50.0$ ,  $110.0$  and  $150.0$ . Similarly, one can construct phase diagrams for other values of the stretching parameter  $\alpha$ .

**Table 1: For different values of  $\alpha$ , minimum values of the arch height for the snap-through and the combined snap-through and pull-in instabilities to occur**

	$\alpha = 50$	$\alpha = 110$	$\alpha = 150$
$h_s$	0.37	0.28	0.23
$h_{sp}$	0.4	0.4	0.4

**Table 2: Comparison of present results with those from the continuum mechanics approach**

	<i>Pull-in voltage</i>	<i>Pull-in displacement</i>	<i>Snap-through voltage</i>	<i>Peak displacement before the snap-through</i>
Present model	Between 95 V and 96 V	11.2 $\mu\text{m}$	Between 65 V and 66 V	2.66 $\mu\text{m}$
Continuum mechanics based analysis [12]	Between 92 V and 93 V	11.0 $\mu\text{m}$	Between 65 V and 66 V	2.60 $\mu\text{m}$
Difference	3.2 %	1.8 %	0 %	2.3 %

### 3.5. Comparison of present results with those from a continuum mechanics approach

In [12] transient finite plane strain electroelastodynamic deformations of a perfect electrically conducting undamped clamped-clamped bell-shaped arch, of the same dimensions and material as the arch in section 2.A, suspended over a flat rigid semi-infinite perfect conductor are analyzed with a continuum mechanics approach. The coupled nonlinear partial differential equations for mechanical deformations are solved numerically by the finite element method and those for the electrical problem by the boundary element method. Effects of geometric nonlinearities are incorporated in the problem formulation and solution; however, structural damping and the damping due to the interaction of the structure with the surrounding medium are neglected. Table 2 compares present results with those reported in [12] for a step potential difference between the two electrodes. It is clear that the present reduced-order model with six degrees of freedom gives results very close to those reported in [12] with thousands of degrees of freedom (recall that the problem in [12] was solved numerically with numerous nodes). For a complex shaped MEMS for which mode shapes are not readily available, one needs to either find mode shapes numerically or use the approach of [12]. The snap-through instability reported in [12] is the direct snap-through instability.

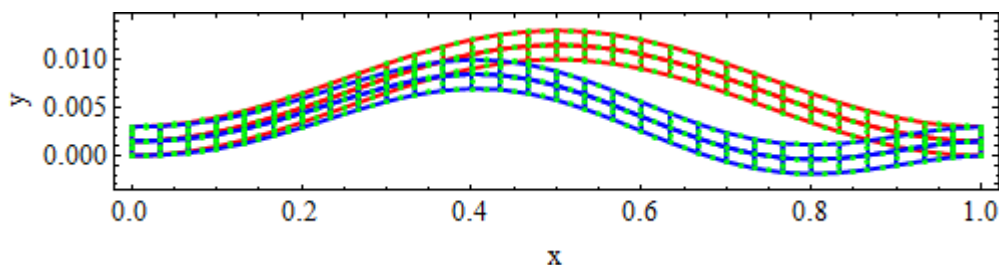


Figure 19. Snap shots of the arch at  $t = 0$  (red) and  $t = 250$  s (blue).

In an attempt to compare asymmetric solutions from the two approaches, we study deformations of a bell shaped silicon arch with base length  $\hat{L} = 1$  mm, width  $\hat{b} = 30$   $\mu\text{m}$ , thickness  $\hat{d} = 3.0$   $\mu\text{m}$ , initial gap  $\hat{g}_0 = 10.0$   $\mu\text{m}$ , the arch rise  $\hat{h} = 10.0$   $\mu\text{m}$ , and its bottom-surface described by  $\hat{z}_0 = \hat{h} \sin^2(\pi \hat{x} / \hat{L})$  using the continuum mechanics approach

described in [12]. The arch experiences the indirect snap-through under step electric potential difference. The critical value of the potential difference for the snap-through instability is between 244 V and 246 V from the continuum mechanics analysis and between 258.0 V and 258.2 V from the present model. The difference of 5% between the two values attests to the adequacy of the present reduced order model. Figure 19 exhibits the arch configurations at two different times obtained from the continuum mechanics formulation of the problem. It is clear that the arch deformed asymmetrically subsequent to the snap-through. Thus, the continuum mechanics approach also predicts the indirect snap-through with deformations of the arch asymmetric about  $x = 0.5$ .

### *3.6. Snap-through and pull-in instabilities under a potential difference linearly varying with time*

The static bifurcation curve ABGB'IJ in figure 20 for an arch with  $h = 0.35$  and  $\alpha = 110$  obtained from the PALC algorithm shows that the arch undergoes both the snap-through instability near point B and the pull-in instability near point I. For low to medium rates (i.e.,  $\leq 25$  V/(unit time)) of increase of  $\beta$ , the arch vibrates around the snapped-through shape until the pull-in occurs. For loading rates  $> 75$  V/(unit time), the snap-through instability is not observed. As the rate of increase of  $\beta$  is decreased the snap-through voltage gradually decreases to 183 V and the pull-in voltage approaches 215 V. It is evident that the snap-through parameters of the arch approach those of the statically deformed arch as the loading rate is decreased. However, the static pull-in voltage exceeds by  $\sim 20\%$  the pull-in voltage for the slowest loading rate considered here.

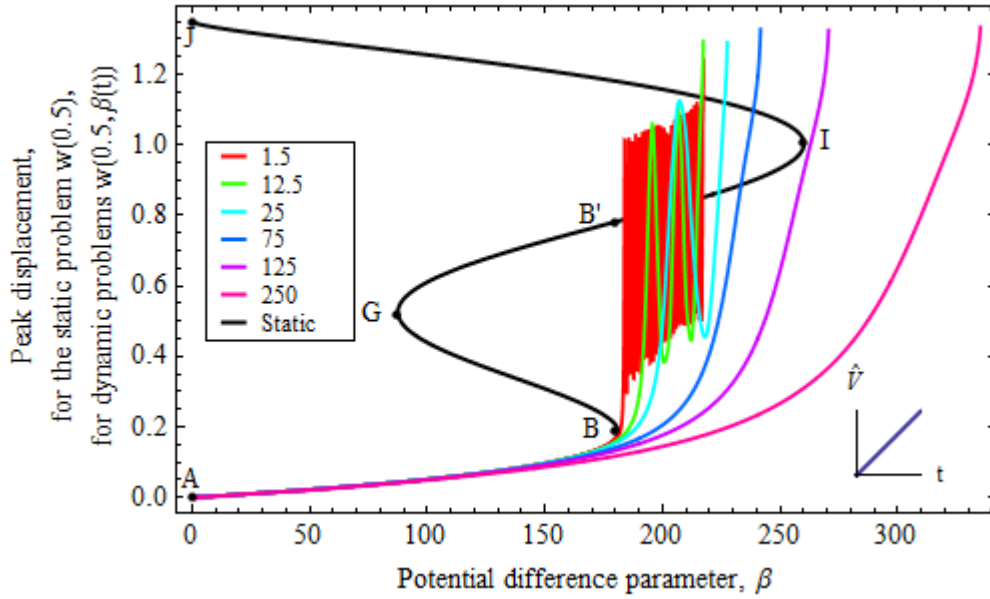


**Figure 20.** For different rates of increase of the applied potential difference ( $V/\text{unit } t$ ) the peak displacement of the mid-span of the arch versus the potential difference parameter  $\beta$ .

Figure 21 exhibits the variation of  $U$  (cf. equation (16)) versus  $\beta$  for dynamic and static problems.  $U$  for dynamic problems follows the curve for the static problem from point A to point B for every rate of increase of  $\beta$ . After point B, the snap-through instability occurs at points  $C_1$ ,  $C_2$  and  $C_3$  for loading rates of 1.5, 12 and 15 ( $V/\text{unit time}$ ), respectively. After the snap-through, the arch vibrates around the new equilibrium position and the potential energy for the dynamic problem always remains higher than that for the static problem (curve B'I in figure 21(c)). For loading rates  $\geq 75$   $V/\text{unit time}$ , the curve  $U$  versus  $\beta$  intersects the curve IJ of  $U$  versus  $\beta$  for the static problem at point P. For loading rates  $\geq 75$  ( $V/\text{unit time}$ ), no snap-through instability is observed. For the loading rate of 75 ( $V/\text{unit time}$ ), the arch experiences the pull-in instability just after its potential energy overshoots the curve IJ. Therefore, the stable motion of the arch under a linearly varying electric potential is observed only when  $U$  for the dynamic problem  $\geq U$  of stable deformations (B'I) for the static problem, and  $\leq U$  of unstable (IJ) deformations of the static problem.

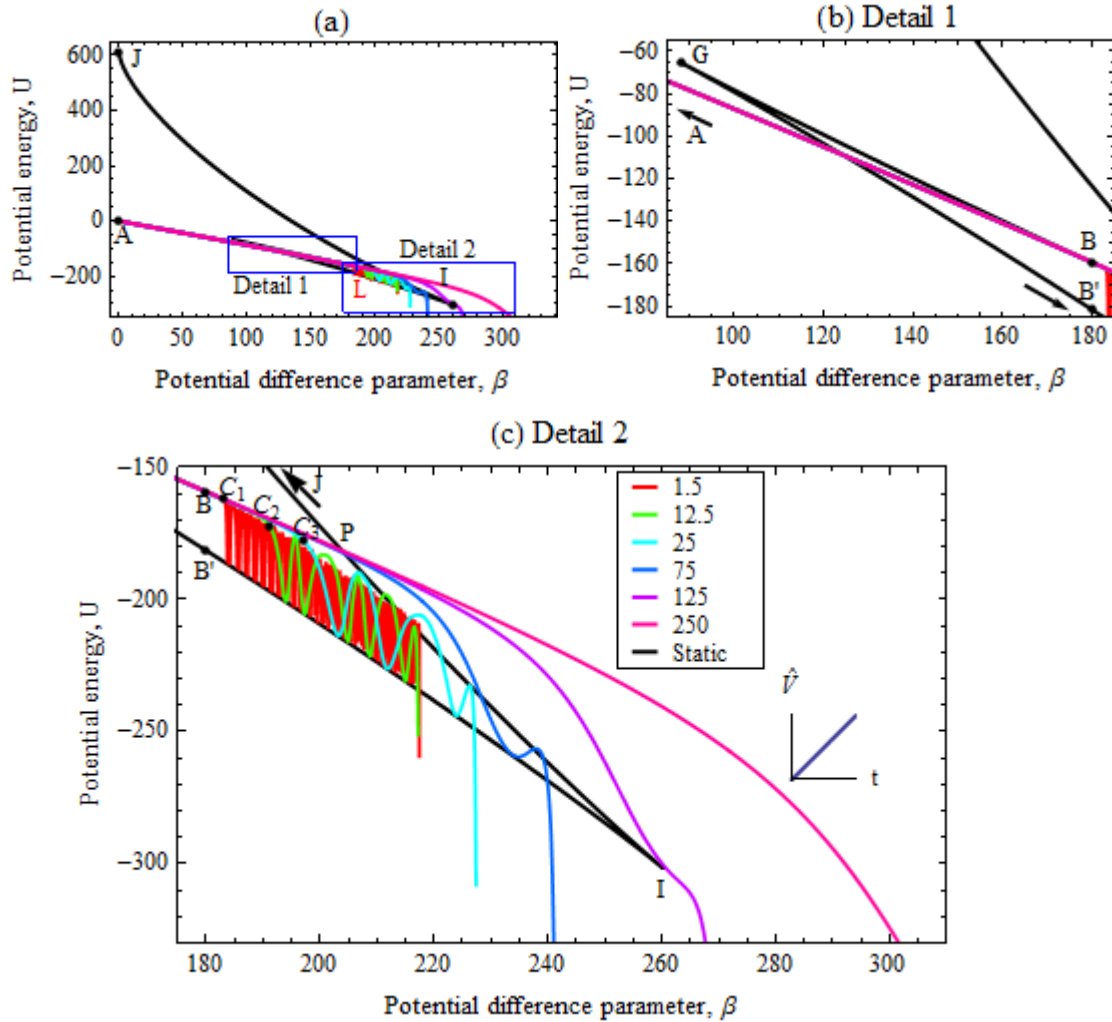


Figure 21. Total potential energy versus the potential difference parameter  $\beta$  for  $h = 0.35$  for the static problem (black curve), the variation of the total potential energy as a function of the potential difference parameter for the dynamic problem when the electric potential is increased linearly with time (colored curves).

### 3.7. Discussion

Simitses [40] has discussed three methods for estimating critical conditions for elastic structures due to transient loads. In the first method governing equations of the problem are solved and a critical condition is reached if a small change in a load parameter causes a large change in the response of the structure. Here, we have solved governing equation (1) using various numerical approaches and estimated the critical values of  $\beta$  for the snap-

through and the pull-in instabilities by monitoring any large change in the peak displacement of the arch for a small change in  $\beta$ .

In the second method, the critical condition of a structure is established by studying the total energy-phase plane for the problem [22, 23], and in the third method the critical load is estimated by analyzing variations of the potential energy due to a small change in the load parameter [45]. The variations of the potential energy of the arch with  $\beta$  for the step electric potential difference reported in the previous sections uses this method for instability analysis.

In [40], the snap-through instability of shallow sinusoidal arches under transient displacement-independent load is studied using a two-mode approximation of the governing equation (6). The pressure over the span of the arch is assumed to vary sinusoidally, and the governing equation is expressed in terms of two non-dimensional parameters, namely, the arch stiffness and the load. The lower and the upper bounds of the critical value of the load parameter for the snap-through instability are studied for the step and impulsive loads.

Deformations of the arch MEMS are governed by four non-dimensional parameters. Instead of quantifying critical values of the load parameter, we have focused on studying mechanisms of instabilities of arches under displacement-dependent electric load.

#### **4. Conclusions**

We have investigated the snap-through and the pull-in instabilities in an electrically actuated micro-arch modeled as an undamped Euler-Bernoulli beam incorporating the nonlinear mid-plane stretching. Two distinct mechanisms, namely the ‘direct’ and the ‘indirect’, snap-through instabilities are found. Whereas the PALC algorithm can compute multiple branches in the bifurcation curve, which correspond to symmetric and asymmetric deformations of the arch, the DIPIE algorithm fails to compute asymmetric solutions.

This work contributes to the theoretical knowledge of the nonlinear behavior and instabilities of a micro-arch under electrical loads, and enables studying bi-stable MEMS. The phase diagram between the critical load parameter and the arch height showing stable and unstable regions of arch's deformations will help in designing arch-shaped MEMS.

Results, including the indirect snap-through and asymmetric deformations subsequent to the snap-through instability from the present reduced order model agree well with those from the continuum mechanics based approach.

Other conclusions are summarized below:

1. An undamped arch under a step electric load may experience either direct or indirect snap-through instability.
2. For relatively small arch heights (e.g., the non-dimensional  $h \leq 0.25$  for  $\alpha = 106$ ), the static problem has solutions with deformations symmetric about the mid-span of the arch and the direct snap-through happens when the locus of the maximum deflection of the dynamic problem intersects the unstable branch of the bifurcation curve for the static problem.
3. For relatively large arch heights (e.g.,  $h > 0.25$  for  $\alpha = 106$ ), the static problem has solutions with deformations symmetric and asymmetric about the mid-span of the arch. The asymmetric solution has lower total potential energy than the corresponding symmetric solution.
4. The indirect snap-through happens when the locus of the maximum deflection of the dynamic problem intersects the unstable branch of the bifurcation curve of the asymmetric deformations for the static problem.
5. For a dynamic problem with the electric potential difference applied as a step function or as a linear function of time, the arch has a stable motion only when its minimum potential energy is  $\geq$  the potential energy of the stable deformed shape of the static problem and  $<$  the potential energy of the unstable deformed shape of the static problem.

## References

- [1] <http://indy.cs.concordia.ca/auto/>.
- [2] 2007 *Bio-MEMS : technologies and applications* (Boca Raton: CRC/Taylor & Francis)
- [3] Ananthasuresh G K, Gupta R K and Senturia S D 1996 An approach to macromodeling of MEMS for nonlinear dynamic simulation *Proceedings of the ASME International Conference of Mechanical Engineering Congress and Exposition (MEMS)*. Atlanta, GA. 401-7
- [4] Bassous E, Taub H H and Kuhn L 1977 Ink jet printing nozzle arrays etched in silicon *Applied Physics Letters* **31** 135-7
- [5] Batra R C, Porfiri M and Spinello D 2006 Analysis of electrostatic MEMS using meshless local Petrov-Galerkin (MLPG) method *Engineering Analysis with Boundary Elements* **30** 949-62
- [6] Batra R C, Porfiri M and Spinello D 2006 Capacitance estimate for electrostatically actuated narrow microbeams *Micro & Nano Letters* **1** 71-3
- [7] Batra R C, Porfiri M and Spinello D 2007 Effects of Casimir force on pull-in instability in micromembranes *Europhysics Letters (EPL)* 20010
- [8] Bochobza-Degani O, Elata D and Nemirovsky Y 2002 An efficient DIPIE algorithm for CAD of electrostatically actuated MEMS devices *Microelectromechanical Systems, Journal of* **11** 612-20
- [9] Budiansky B and Hutchinson J W 1964 Dynamic buckling of imperfection sensitive structure *TR 18, Contract 1866 (02), Div of Engineering and Applied Physics, Harvard Univ. (June 164) and AIAA J* **4** 525-30
- [10] Chao P C-P, Chiu C W and Liu T-H 2008 DC dynamic pull-in predictions for a generalized clamped-clamped micro-beam based on a continuous model and bifurcation analysis *Journal of Micromechanics and Microengineering* **18** 0960-1317
- [11] Chu P B, Nelson P R, Tachiki M L and Pister K S J 1996 Dynamics of polysilicon parallel-plate electrostatic actuators *Sensors and Actuators A: Physical* **52** 216-20
- [12] Das K and Batra R C Pull-in and snap-through instabilities in transient deformations of microelectromechanical Systems *submitted to the Journal of Micromechanics and Microengineering*
- [13] Doedel E, Keller H B and Kernevez J P 1991 Numerical analysis and control of bifurcation problems *International Journal of Bifurcation and Chaos* **1** 493 - 520
- [14] Flores G, Mercado G A and Pelesko J A 2003 Dynamics and touchdown in electrostatic MEMS. In: *MEMS, NANO and Smart Systems, 2003. Proceedings. International Conference on*, pp 182-7
- [15] Fujii F 1989 Scheme for elasticas with snap-back and looping *Journal of Engineering Mathematics* **115** 2166-81
- [16] Ganapathi M, Gupta S S and Patel B P 2003 Nonlinear axisymmetric dynamic buckling of laminated angle-ply composite spherical caps *Composite Structures* **59** 89-97



- [17] Goll C, Bacher W, Buestgens B, Maas D, Menz W and Schomburg W K 1996 Microvalves with bistable buckled polymer diaphragms *Journal of Micromechanics and Microengineering* 77-9
- [18] Gupta S S, Patel B P and Ganapathi M 2003 Nonlinear dynamic buckling of laminated angle-ply composite spherical caps *Journal of Structural Engineering and Mechanics* **15** 463-76
- [19] Humphreys J S 1966 On dynamic snap buckling of shallow arches *AIAA Journal* **4** 878-86
- [20] Hung E S and Senturia S D 1999 Extending the travel range of analog-tuned electrostatic actuators *Microelectromechanical Systems, Journal of* **8** 497-505
- [21] Krylov S, Bojan R I, David S, Shimon S and Harold C 2008 The pull-in behavior of electrostatically actuated bistable microstructures *Journal of Micromechanics and Microengineering* 055026
- [22] Krylov S and Maimon R 2004 Pull-in Dynamics of an Elastic Beam Actuated by Continuously Distributed Electrostatic Force *Journal of Vibration and Acoustics* **126** 332-42
- [23] Krylov S, Serentensky S and Schreiber D 2007 Pull-in behavior of electrostatically actuated multistable microstructures. In: *ASME 2007 International Design Engineering Technical Conference & Computers and Information in Engineering Conference*, (Las Vegas, Nevada, USA
- [24] Krylov S, Seretensky S and Schreiber D 2008 Pull-in behavior and multistability of a curved microbeam actuated by a distributed electrostatic force. In: *Micro Electro Mechanical Systems, 2008. MEMS 2008. IEEE 21st International Conference on*, ed S Seretensky pp 499-502
- [25] Kugel V D, Xu B, Zhang Q M and Cross L E 1998 Bimorph-based piezoelectric air acoustic transducer: model *Sensors and Actuators A: Physical* **69** 234-42
- [26] Legtenberg R and Tilmans H A C 1994 Electrostatically driven vacuum-encapsulated polysilicon resonators Part I. Design and fabrication *Sensors and Actuators A: Physical* **45** 57-66
- [27] Lock M H 1966 Snapping of a shallow sinusoidal arch under a step pressure load *AIAA Journal* **4** 1249-56
- [28] Nathanson H C, Newell W E, Wickstrom R A and Davis J R, Jr. 1967 The resonant gate transistor *Electron Devices, IEEE Transactions on* **14** 117-33
- [29] Nayfeh A, Younis M and Abdel-Rahman E 2007 Dynamic pull-in phenomenon in MEMS resonators *Nonlinear Dynamics* **48** 153-63
- [30] Nguyen C T C, Katehi L P B and Rebeiz G M 1998 Micromachined devices for wireless communications *Proceedings of the IEEE* **86** 1756-68
- [31] Park S and Hah D 2008 Pre-shaped buckled-beam actuators: Theory and experiments *Sensors and Actuators A: Physical* **148** 186-92
- [32] Patricio P, Adda-Bedia M and Ben Amar M 1998 An elastica problem: instabilities of an elastic arch *Physica D: Nonlinear Phenomena* **124** 285-95
- [33] Pelesko J A, Bernstein D H and McCuan J 2003 Symmetry and Symmetry Breaking in Electrostatically Actuated MEMS *Nanotech* **2** 432 - 5
- [34] Pippard A B 1990 The elastic arch and its modes of instability *European Journal of Physics* 359-65

- [35] Postma H W C, Kozinsky I, Husain A and Roukes M L 2005 Dynamic range of nanotube- and nanowire-based electromechanical systems *Applied Physics Letters* **86** 223105
- [36] Radhakrishnan K and Hindmarsh. A C 1993 *Description and use of LSODE : the Livermore solver for ordinary differential equations* (Springfield, VA: National Aeronautics and Space Administration, Office of Management, Scientific and Technical Information Program)
- [37] Rebeiz G M 2003 RF MEMS theory, design, and technology. (Hoboken, NJ: John Wiley & Sons, Inc.)
- [38] Roylance L M and Angell J B 1979 A batch-fabricated silicon accelerometer *Electron Devices, IEEE Transactions on* **26** 1911-7
- [39] Saif M T A 2000 On a tunable bistable MEMS-theory and experiment *Microelectromechanical Systems, Journal of* **9** 157-70
- [40] Simitses G J 1990 *Dynamic Stability of Suddenly Loaded Structures* (New York: Springer-Verlag)
- [41] Taylor G 1968 The Coalescence of Closely Spaced Drops when they are at Different Electric Potentials *Proceedings of the Royal Society of London. Series A, Mathematical and Physical Sciences* **306** 423-34
- [42] Van Kessel P F, Hornbeck L J, Meier R E and Douglass M R 1998 A MEMS-based projection display *Proceedings of the IEEE* **86** 1687-704
- [43] Vangbo M 1998 An analytical analysis of a compressed bistable buckled beam *Sensors and Actuators A: Physical* **69** 212-6
- [44] Vangbo M and Bcklund Y 1998 A lateral symmetrically bistable buckled beam *Journal of Micromechanics and Microengineering* **8** 29-32
- [45] Xu Z and Mirmiran A 1997 Looping behavior of arches using corotational finite element *Computers & Structures* **62** 1059-71
- [46] Zhang Y, Wang Y, Li Z, Huang Y and Li D 2007 Snap-Through and Pull-In Instabilities of an Arch-Shaped Beam Under an Electrostatic Loading *Microelectromechanical Systems, Journal of* **16** 684-93